

A Treatise on Potential Energy

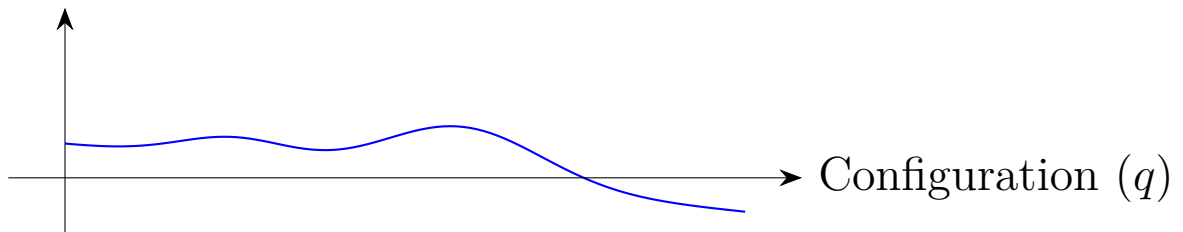
Diagrams in Physics

A Historical and Pedagogical Review

Onri Jay Benally

August 2025

The Landscape of Possibility
Potential Energy (U)



Contents

1	Introduction: The Enduring Metaphor of the Hill	3
2	A Brief Primer	5
2.1	Energy Hills Act Like Gravity Hills	5
2.2	Barriers in Chemistry Play the Same Role	6
2.3	Quantum Particles Sometimes “Cheat”	7
2.4	Modern Chips Still Draw Hills	7
3	A Historical Trajectory	7
3.1	Classical and Early Analytical Mechanics (1740 – 1870)	8
3.2	Chemical Kinetics and the “Activation Hill” (1884 – 1930)	8
3.3	Quantum Tunneling Barriers (1928 – 1950)	10
3.4	Semiconductor Band & Junction Diagrams (1930 – present)	12
3.5	Macroscopic Quantum Devices (1980 – present)	13
4	Mathematical Formalism and Stability Analysis	18
4.1	Force–Potential Relations in One and Many Dimensions	18
4.2	Equilibria, Hessian, and Stability (Morse Classification)	18
4.3	Small Oscillations and Normal Modes	19
4.4	Semiclassical Tunneling (Wentzel–Kramers–Brillouin)	20
4.5	Transition-State Theory (TST) and Kramers Escape	21
4.6	Electrostatics of a p–n Junction: Built-in Potential and Width	23
4.7	Josephson Junction Dynamics	24
4.8	Landau Expansions Near Symmetry Breaking	27
4.9	Minimum-Energy Paths on Multidimensional Surfaces (NEB Sketch)	30
5	Evolution of Diagrammatic Conventions	32

6 Conceptual Connections and Glossary	33
6.1 Mind-Map of Concepts	33
6.2 Diagrammatic Cousins: Heat Maps	34
7 Formula Sheet: Barriers, Rates, and Wells	36
7.1 Acronym Glossary	37
8 Conclusion: A Representation Agnostic Vision	38

1 Introduction: The Enduring Metaphor of the Hill

In the long arc of physics, thinkers have repeatedly sketched “hills” and “walls” of potential energy so that our eyes—and therefore our intuition—can follow how a particle, charge-carrier, or chemical complex might move. This visual metaphor, rooted in our everyday experience with gravity, has proven to be remarkably versatile and enduring. Starting with gravity-like drawings for springs and projectiles, progressing through chemical “activation hills,” quantum-mechanical tunneling barriers, semiconductor band steps, and today’s tilted-washboard landscapes for Josephson circuits, the diagram style has steadily evolved, yet the underlying concept has stayed the same: a vertical axis of energy, a horizontal axis of configuration, and arrows that announce motion “up-and-over” or, more subtly, “through” the barrier when quantum physics allows.

The power of this diagrammatic approach lies in its ability to translate abstract mathematical relationships into a tangible, graphical landscape. The shape of a curve on a page immediately conveys concepts of stability, transition, and confinement that would otherwise require pages of equations to describe. It is a tool for both pedagogy and research, allowing students to build intuition and experts to frame complex problems.

This document explores the history, application, and pedagogical power of the potential energy diagram. We will begin with a primer suitable for early students, tracing the core analogy to a simple gravitational hill. We will then embark on a more expansive graduate-level analysis, examining the key historical milestones where this diagrammatic tool was adapted to new domains of physics, from chemical kinetics to quantum computing. We will introduce new diagrams to illustrate these advanced concepts, delve into the mathematical formalism that underpins them, and present a series of tables and conceptual maps to summarize the evolution of these conventions. The goal is to create a comprehensive reference on this foundational tool of theoretical physics, demonstrating its breadth and its continued relevance in modern science.

Roadmap. Section 2 builds the hill metaphor at a high-school level; Section 3 follows the historical re-targeting of the diagram across mechanics, chemistry, quantum tunneling, semiconductor bands, and macroscopic quantum devices; Section 4 then anchors the pictures in force–potential relations, Hessian stability, and standard barrier-crossing approximations; Section 5 summarizes how the visual conventions themselves evolved; Section 6 provides a compact conceptual map; and Section 7 closes with a formula sheet and acronym glossary.

2 A Brief Primer

At its heart, the potential energy diagram is a simple idea that leverages our intuition about the physical world. The core concepts can be grasped with four key points, each building on the last.

2.1 Energy Hills Act Like Gravity Hills

When you see a hump on a potential-energy graph, one can imagine trying to push a ball over an earthly hill. Gravity resists your effort, so you must supply extra push, which translates to kinetic energy. In the diagram, that “extra push” is the energy difference between the particle’s total energy and the peak of the potential hill. If the particle’s energy is greater than the hill’s peak, it rolls over; if not, it rolls back. This simple, powerful analogy is often the first introduction students have to the concept for systems like springs, planets, and electrons, precisely because the connection to gravity is so familiar and intuitive. In this one-dimensional case, the horizontal axis x is a simple configuration coordinate; later we will generalize to a vector of coordinates \mathbf{q} that jointly describe a system’s configuration space.

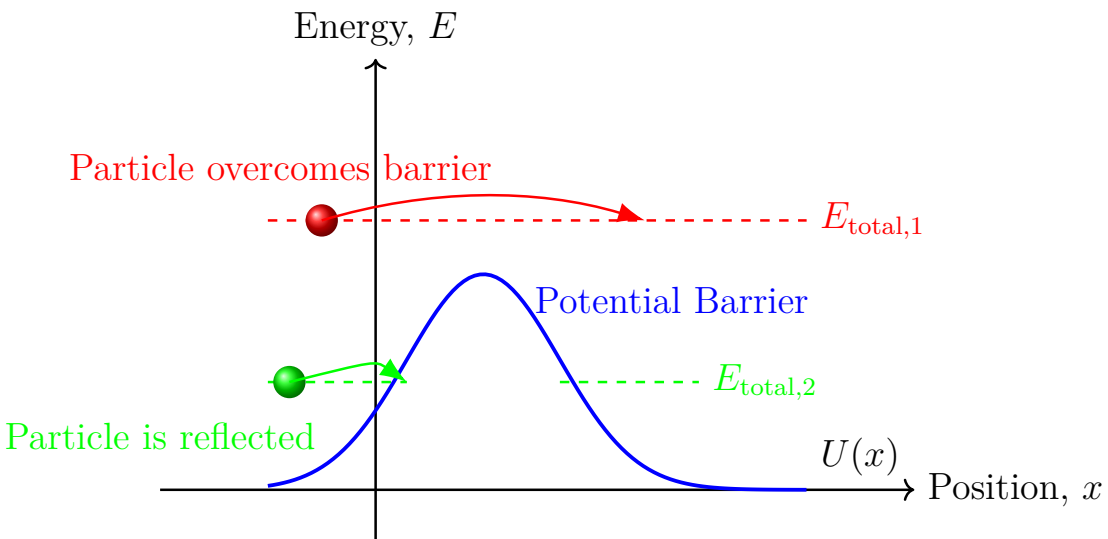


Figure 1: A classical potential energy hill. A particle with total energy $E_{\text{total},1}$ (red) can pass over the barrier, while a particle with energy $E_{\text{total},2}$ (green) is confined to the region left of the hill.

2.2 Barriers in Chemistry Play the Same Role

The analogy extends directly to chemistry. For a chemical reaction to occur, reactant molecules must collide with sufficient energy to overcome an energetic barrier and rearrange into products. This minimum energy is called the **activation energy** (E_a), a concept famously captured by the Arrhenius equation in 1889. For many thermally activated processes the empirical rate law can be written as

$$k(T) = A \exp\left(-\frac{E_a}{RT}\right),$$

which makes the energetic hill appear directly in the exponential suppression factor. A reaction coordinate diagram, which plots energy versus the progress of a reaction, shows this activation energy as a hill that separates reactants from products.

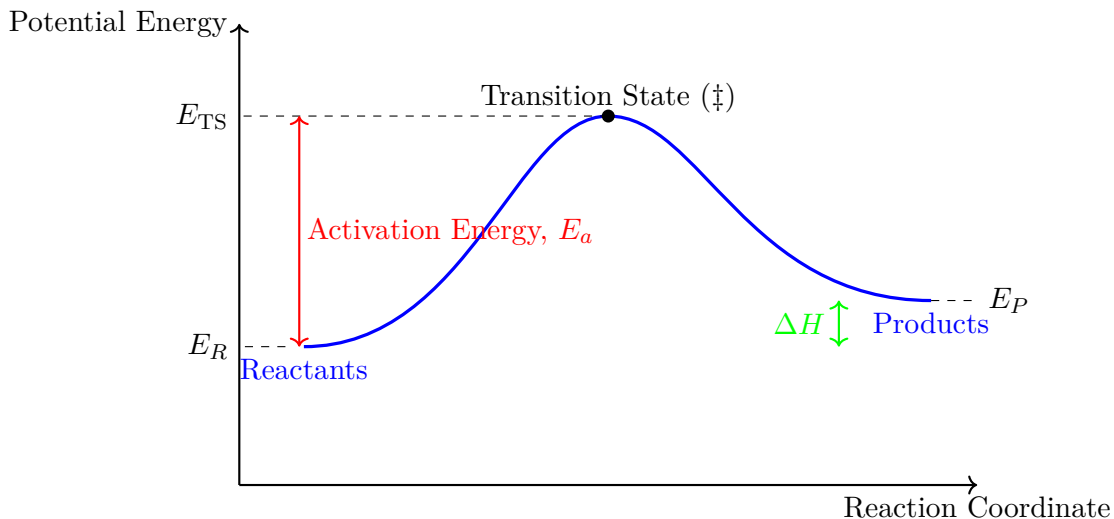


Figure 2: A reaction coordinate diagram for an endothermic reaction. Reactants must gain the activation energy (E_a) to reach the transition state before forming products. The overall change in enthalpy (ΔH) is positive.

2.3 Quantum Particles Sometimes “Cheat”

The classical world is deterministic in this regard: not enough energy means you cannot cross. The quantum world, however, is probabilistic. In 1928, George Gamow explained the phenomenon of alpha decay by showing that an alpha particle can **tunnel through** a nuclear potential barrier even if it classically lacks the energy to go over it. This revolutionary idea meant that arrows in quantum diagrams could now slice straight through the wall, representing a classically forbidden process made possible by the wave-like nature of particles. Mathematically, in a region where $U(x) > E$ the time-independent Schrödinger equation implies a solution of the form $\psi(x) \propto \exp[-\kappa x]$ with $\kappa > 0$, so the probability density decays inside the barrier yet remains non-zero on the far side.

2.4 Modern Chips Still Draw Hills

The hill metaphor remains central in cutting-edge technology. In superconducting quantum bits (qubits), the state of the system is described by the phase of a quantum wavefunction, which sits in a potential energy landscape. For a Josephson junction, this landscape is often a “tilted washboard” potential. Engineers can tune an external bias current to tilt this washboard, effectively lowering or raising the hills between adjacent wells, which allows them to control the quantum state of the qubit. This qualitative picture is developed into a full mathematical model in Section 4 and, in particular, in the RCSJ description of Josephson junction dynamics in Section 4.7.

3 A Historical Trajectory

The potential energy diagram is not a static concept but one that has been refined and repurposed over nearly two centuries of physics. Its evolution tracks the major theoretical developments in the field.

3.1 Classical and Early Analytical Mechanics (1740 – 1870)

While the concept of potential energy was formalized by Lagrange in his *Mécanique analytique* [1], the initial formulations were purely algebraic. Early thinkers like Bernoulli and Lagrange worked with expressions of kinetic minus potential energy ($T - U$) without the aid of graphical representation.

It was not until the mid-19th century that textbook authors, notably William Rankine and later James Clerk Maxwell [2], began to plot potential energy $U(x)$ against a configuration coordinate x . These early diagrams were used to illustrate fundamental concepts such as stable and unstable equilibrium points and the nature of simple harmonic motion. A particle placed at a local minimum of a potential well would oscillate, while a particle placed at a maximum would be in unstable equilibrium, ready to roll down the hill. This marked the birth of the potential energy diagram as a pedagogical tool.

3.2 Chemical Kinetics and the “Activation Hill” (1884 – 1930)

The application of energy diagrams to chemistry began with the work of Jacobus Henricus van ’t Hoff and Svante Arrhenius. By studying the temperature dependence of reaction rates, they inferred that most reactions face a fixed energy obstacle. Arrhenius proposed his famous equation [3],

$$k = Ae^{-E_a/(RT)} \quad (1)$$

where k is the reaction rate constant, A is a pre-exponential factor, R is the gas constant, T is the absolute temperature, and E_a is the activation energy. This equation mathematically described the “hill” that reactants must climb.

This picture was formalized in 1935 with the development of **Transition State Theory (TST)** by Henry Eyring, Meredith Gwynne Evans, and Michael Polányi [4]. TST posits that a quasi-equilibrium exists between reactants and an activated complex at the peak of the energy barrier, known as the transition state. Diagrams from this era are often marked

with a double dagger (\ddagger) at the peak to signify this special configuration, as shown previously in Figure 2.

3.3 Quantum Tunneling Barriers (1928 – 1950)

The classical paradigm of insurmountable barriers was shattered with the advent of quantum mechanics. The puzzle of alpha decay—how an alpha particle could escape the strong nuclear force holding it within a nucleus—was solved independently by George Gamow [5] and by Ronald Gurney and Edward Condon [6] in 1928. They modeled the nucleus as a potential well surrounded by a high Coulomb barrier. Classically, an alpha particle with an energy below the barrier peak would be trapped forever. Quantum mechanically, however, the particle’s wavefunction does not abruptly go to zero at the barrier wall. Instead, it decays exponentially inside the barrier. If the barrier is thin enough, the wavefunction has a small but non-zero amplitude on the other side, implying a finite probability of escape. This phenomenon was named **quantum tunneling**.

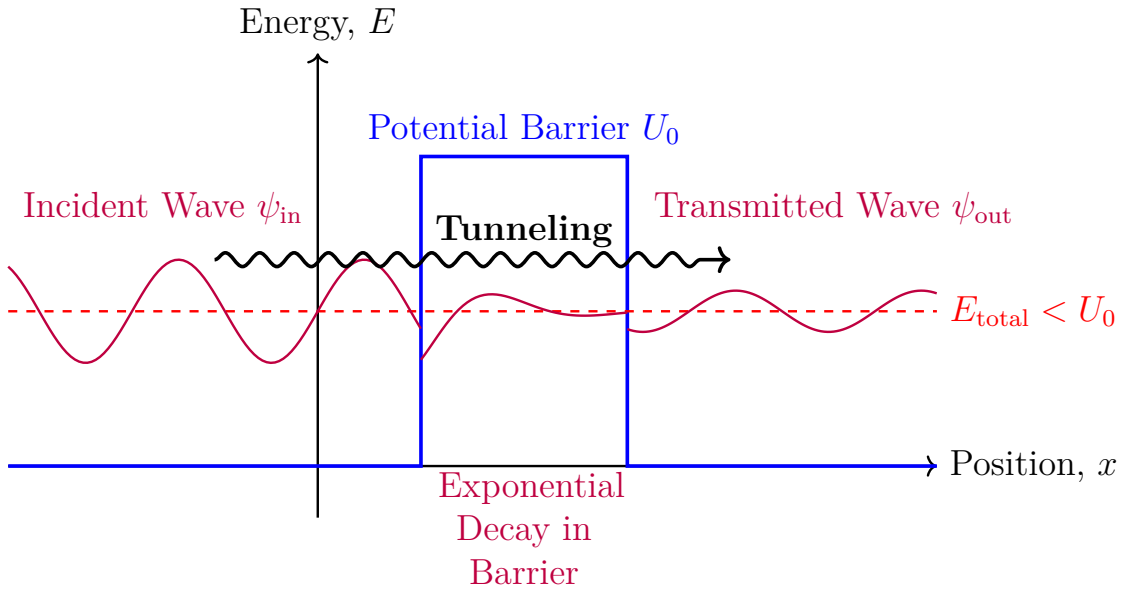


Figure 3: Quantum tunneling through a potential barrier. The particle’s wavefunction (purple) has a non-zero amplitude after the barrier, indicating a probability of transmission even though its energy E_{total} is less than the barrier height U_0 .

The mathematical basis for this is the time-independent Schrödinger equation:

$$-\frac{\hbar^2}{2m} \frac{d^2\psi(x)}{dx^2} + U(x)\psi(x) = E\psi(x). \quad (2)$$

In a classically forbidden region where $U(x) > E$, the solution for $\psi(x)$ is no longer oscillatory but takes the form of a real exponential decay. The semi-classical **Wentzel–Kramers–Brillouin (WKB)** approximation provided a powerful tool for calculating tunneling probabilities for barriers of arbitrary shape.

3.4 Semiconductor Band & Junction Diagrams (1930 – present)

A parallel evolution of energy diagrams occurred in solid-state physics. The quantum theory of solids, developed in the 1930s, introduced the concept of electronic **band structure**. When two different types of semiconductors (p-type and n-type) are brought together to form a p-n junction, the band energies must align to create a constant Fermi level, resulting in **band bending**. This creates a potential barrier at the junction that is essential for the rectifying behavior of diodes [9]. The gravitational analogy persists here: electrons are said to “roll downhill” from high conduction-band edges to low ones.

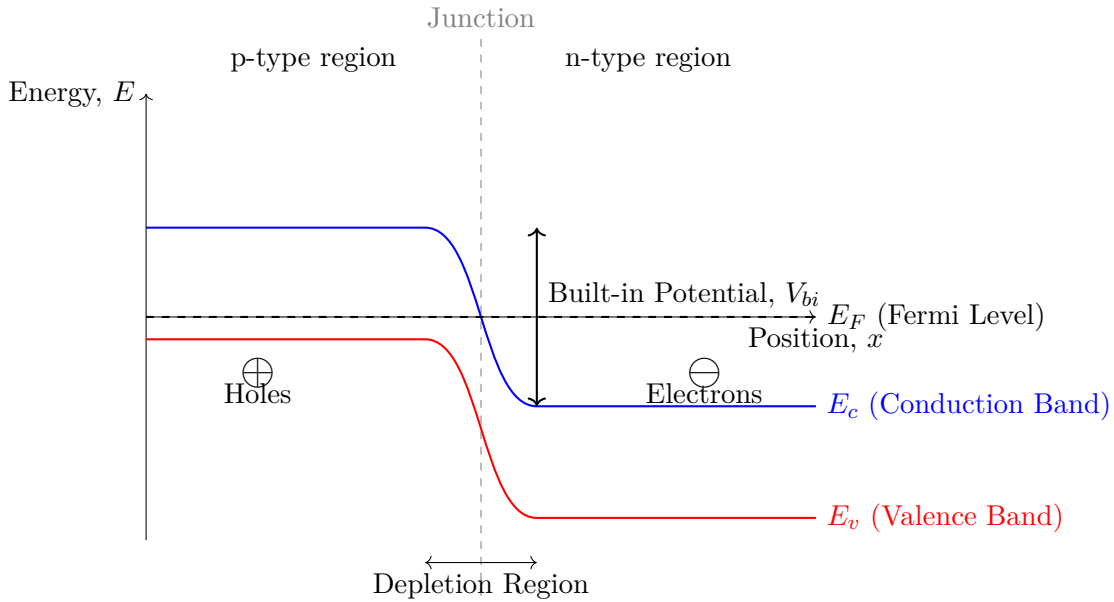


Figure 4: A band diagram for a p-n junction at equilibrium. Band bending creates a potential barrier that prevents the net flow of charge carriers across the junction.

For a quantitative link to dopants, permittivity, and barrier width, see Section 4.6.

3.5 Macroscopic Quantum Devices (1980 – present)

In the late 20th century, physicists began to build devices where macroscopic variables behave quantum mechanically. A prime example is the **Josephson junction** [10, 11], formed by two superconductors separated by a thin insulating layer. The dynamics of the quantum phase difference ϕ across the junction can be described by a particle moving in a potential given by:

$$U(\phi) = -E_J \cos(\phi) - \frac{\hbar I_b}{2e} \phi \quad (3)$$

where E_J is the Josephson energy and I_b is an external bias current. This is famously known as the **tilted-washboard potential**. By adjusting the tilt (I_b), one can trap the “phase particle” in a well or allow it to escape, forming the basis of superconducting qubits.

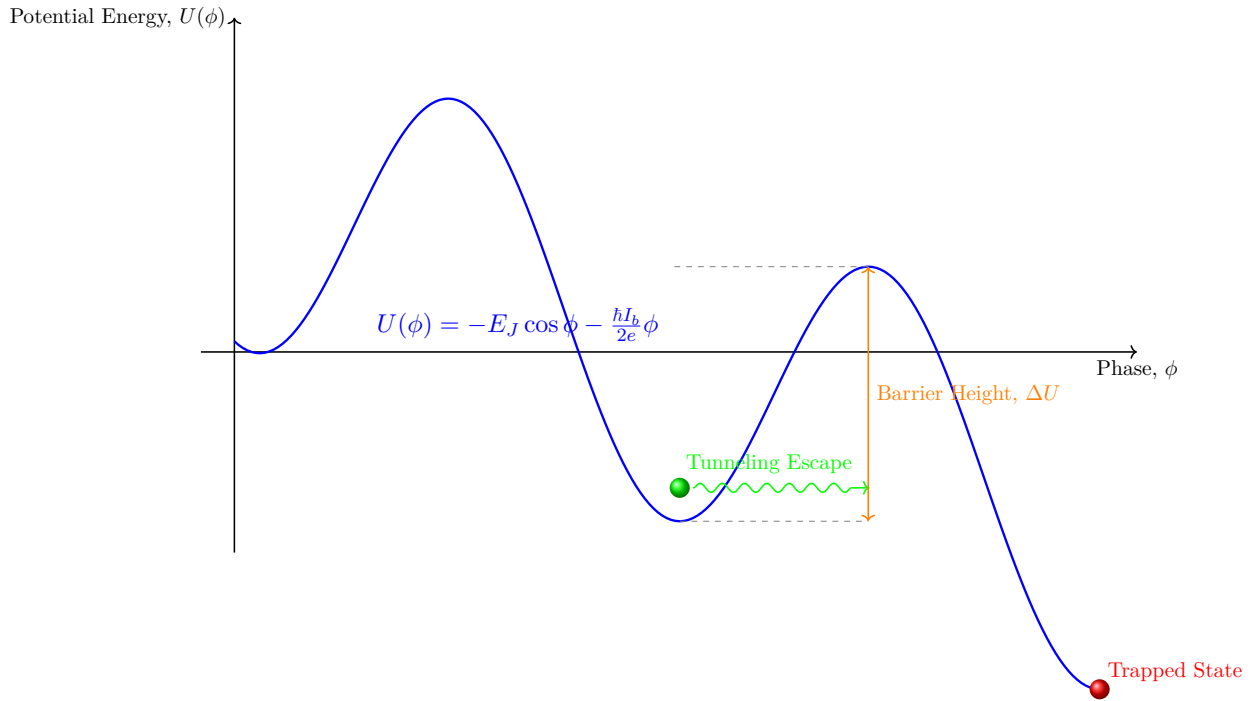


Figure 5: The tilted-washboard potential for a Josephson junction. A quantum state can be trapped in a potential well or can escape via quantum tunneling. The barrier height ΔU is shown relative to the well from which tunneling occurs.

A second archetype of macroscopic (or mesoscopic) quantum device is the **double-well potential** realized in superconducting flux qubits and in semiconductor double quantum

dots. In a simple one-dimensional model,

$$U(x) = ax^4 - bx^2 - fx, \quad a > 0, b > 0, \quad (4)$$

the competition between the quartic and quadratic terms generates two minima separated by a barrier, and the linear term fx acts as a controllable tilt. The two lowest eigenstates are symmetric and antisymmetric superpositions of left- and right-localized states, with an energy splitting determined by the tunneling matrix element. In semiconductor implementations, electrostatic gate voltages effectively shape $U(x)$, while in flux qubits the bias is the external magnetic flux; in both cases the potential-energy diagram provides an immediate picture of the qubit's logical states and the controllable barrier between them.

A third modern family uses **effective potentials for photons and phonons** in nanoscale metamaterial waveguides and quantum transducers [15, 16]. In the paraxial and slowly-varying-envelope approximations, the complex field envelope $A(x, z)$ in a structured waveguide can be shown to satisfy a Schrödinger-like equation of the form

$$i \frac{\partial A}{\partial z} = -\frac{1}{2k_0 n_0} \frac{\partial^2 A}{\partial x^2} + V_{\text{eff}}(x) A, \quad (5)$$

where z plays the role of “time” and the effective potential $V_{\text{eff}}(x)$ is determined by the refractive-index landscape of the meta-waveguide. Regions of higher effective index act as potential wells that confine optical modes, whereas engineered index variations create barriers and bandgaps that mimic multi-well quantum potentials.

Worked Example 3.1 (Bound mode in an effective-index well). High-level idea.

We solve for a guided optical mode in a simple symmetric effective-index well using Eq. (5). This mirrors how one finds a bound state of a quantum particle in a finite square well, but now the “particle” is an optical field envelope and the propagation coordinate z plays the role of time.

Derivation. We look for modes of the form

$$A(x, z) = u(x) e^{i\beta z}, \quad (6)$$

where β is the propagation constant (the analogue of an energy eigenvalue). Inserting Eq. (6) into Eq. (5) gives

$$\beta u(x) = -\frac{1}{2k_0 n_0} \frac{d^2 u}{dx^2} + V_{\text{eff}}(x) u(x), \quad (7)$$

which is an eigenvalue problem for $u(x)$.

Consider a symmetric “slab” effective index profile,

$$V_{\text{eff}}(x) = \begin{cases} 0, & |x| < a, \\ V_0 > 0, & |x| > a, \end{cases} \quad (8)$$

which plays the role of a finite square well: lower effective potential inside the core, higher outside.

Step 1: Solutions inside and outside the core. Inside the core ($|x| < a$), $V_{\text{eff}}(x) = 0$, so Eq. (7) reduces to

$$-\frac{1}{2k_0 n_0} \frac{d^2 u}{dx^2} = \beta u(x), \quad (9)$$

or

$$\frac{d^2 u}{dx^2} + 2k_0 n_0 \beta u(x) = 0. \quad (10)$$

Define

$$k \equiv \sqrt{2k_0 n_0 \beta}, \quad (11)$$

and the general solution inside the core is

$$u_{\text{in}}(x) = A \cos(kx) + B \sin(kx), \quad |x| < a. \quad (12)$$

Outside the core ($|x| > a$), $V_{\text{eff}}(x) = V_0$, so Eq. (7) becomes

$$-\frac{1}{2k_0 n_0} \frac{d^2 u}{dx^2} + V_0 u(x) = \beta u(x), \quad (13)$$

or

$$\frac{d^2 u}{dx^2} = 2k_0 n_0 (V_0 - \beta) u(x). \quad (14)$$

For a guided (bound) mode we require $0 < \beta < V_0$, so that $V_0 - \beta > 0$. Define

$$\alpha \equiv \sqrt{2k_0 n_0 (V_0 - \beta)}, \quad (15)$$

and take exponentially decaying solutions:

$$u_{\text{out}}(x) = \begin{cases} C e^{-\alpha(x-a)}, & x > a, \\ C e^{+\alpha(x+a)}, & x < -a, \end{cases} \quad (16)$$

where symmetry has already been anticipated (see below).

Step 2: Even fundamental mode and matching conditions. For the lowest-order guided mode in a symmetric structure, we expect an even profile, so we set $B = 0$ in Eq. (12) and choose symmetric decays outside. Thus

$$u_{\text{in}}(x) = A \cos(kx), \quad u_{\text{out}}(x) = \begin{cases} C e^{-\alpha(x-a)}, & x > a, \\ C e^{+\alpha(x+a)}, & x < -a. \end{cases} \quad (17)$$

Continuity of $u(x)$ and du/dx at $x = a$ gives

$$u_{\text{in}}(a) = u_{\text{out}}(a), \quad (18)$$

$$u'_{\text{in}}(a) = u'_{\text{out}}(a). \quad (19)$$

From Eq. (18),

$$A \cos(ka) = C, \quad (20)$$

and from Eq. (19),

$$-Ak \sin(ka) = -\alpha C. \quad (21)$$

Eliminating A and C leads to the transcendental condition

$$k \tan(ka) = \alpha, \quad (22)$$

with

$$k^2 = 2k_0 n_0 \beta, \quad \alpha^2 = 2k_0 n_0 (V_0 - \beta). \quad (23)$$

Equation (22) is the dispersion relation for the even (fundamental) guided mode of this effective-index well. Given physical parameters (k_0, n_0, V_0, a) one solves Eq. (22) for β , which determines both the propagation constant and the detailed mode profile $u(x)$.

This worked example shows that, in the metamaterial setting, the “mode Hill” in $V_{\text{eff}}(x)$ plays exactly the same mathematical role as a quantum-mechanical potential well: guided optical modes are bound states of the effective Schrödinger equation (5), with a discrete spectrum of allowed β values set by boundary and continuity conditions.

In hybrid electro- or piezo-optomechanical quantum transducers, a mechanical displacement coordinate is coupled to both microwave and optical fields; the corresponding effective potential for the mechanical mode can develop multiple minima and barrier crossings, again making potential-energy diagrams a natural language for understanding conversion pathways and stability regimes.

For the full RCSJ dynamics, plasma frequency, and escape-rate formulas in the Josephson case, see Section 4.7.

4 Mathematical Formalism and Stability Analysis

Because intuition benefits from precise anchors, and because diagrams deserve equations that certify the picture, we now set the rigorous footing. Throughout, e denotes the elementary charge, $\hbar = h/2\pi$, k_B is Boltzmann's constant, and $\Phi_0 = h/2e$. Unless otherwise noted we use SI units.

Standing assumptions. Unless otherwise stated, we take the configuration space to be \mathbb{R}^n with generalized coordinates \mathbf{q} ; the potential $U : \mathbb{R}^n \rightarrow \mathbb{R}$ is at least twice continuously differentiable (C^2); the force field is conservative, $\mathbf{F}(\mathbf{q}) = -\nabla U(\mathbf{q})$; and any mass matrix M that appears is symmetric positive definite. These mild smoothness and positivity assumptions are enough to justify the Hessian-based stability classification and normal-mode analysis that follow.

4.1 Force–Potential Relations in One and Many Dimensions

In one dimension, a conservative force is the negative slope of the potential:

$$F(x) = -\frac{dU(x)}{dx}. \quad (24)$$

In n dimensions with generalized coordinates $\mathbf{q} \in \mathbb{R}^n$,

$$\mathbf{F}(\mathbf{q}) = -\nabla U(\mathbf{q}), \quad \nabla = \begin{bmatrix} \partial/\partial q_1 & \dots & \partial/\partial q_n \end{bmatrix}^\top. \quad (25)$$

4.2 Equilibria, Hessian, and Stability (Morse Classification)

Equilibria satisfy $\nabla U(\mathbf{q}_*) = \mathbf{0}$. The second-derivative matrix,

$$H(\mathbf{q}_*) = \nabla^2 U(\mathbf{q}_*) \in \mathbb{R}^{n \times n}, \quad (26)$$

classifies the equilibrium:

- **Strict local minimum (nonlinear Lyapunov stable):** H positive definite (all eigenvalues > 0).
- **Saddle:** H indefinite (one or more negative eigenvalues); the number of negative eigenvalues is the *Morse index*.
- **Local maximum (unstable):** H negative definite (all eigenvalues < 0).

For a conservative mechanical system with kinetic energy $T = \frac{1}{2}\dot{\mathbf{q}}^\top M\dot{\mathbf{q}}$ and potential U , the total energy $E = T + U$ is a Lyapunov function. If $H(\mathbf{q}_*)$ is positive definite, then \mathbf{q}_* is a strict local energy minimum and therefore Lyapunov stable; saddles and maxima are locally energetically unstable. Under the smoothness assumptions above, nondegenerate critical points (those with $\det H(\mathbf{q}_*) \neq 0$) are Morse critical points; the Morse index is exactly the number of negative eigenvalues of $H(\mathbf{q}_*)$.

4.3 Small Oscillations and Normal Modes

Near a stable equilibrium \mathbf{q}_* , write $\mathbf{q} = \mathbf{q}_* + \boldsymbol{\eta}$. With kinetic energy $T = \frac{1}{2}\dot{\boldsymbol{\eta}}^\top M\dot{\boldsymbol{\eta}}$ (constant mass matrix M evaluated at \mathbf{q}_*) and $U(\mathbf{q}) \approx U(\mathbf{q}_*) + \frac{1}{2}\boldsymbol{\eta}^\top H\boldsymbol{\eta}$, the linearized equations become

$$M\ddot{\boldsymbol{\eta}} + H\boldsymbol{\eta} = \mathbf{0}. \quad (27)$$

Seeking $\boldsymbol{\eta}(t) = \mathbf{v}e^{i\omega t}$ yields the generalized eigenproblem

$$H\mathbf{v} = \omega^2 M\mathbf{v}, \quad (28)$$

so the normal-mode frequencies are $\omega_i = \sqrt{\lambda_i}$ where λ_i are the generalized eigenvalues of (H, M) . Because M is symmetric positive definite and H is symmetric, one can always transform to mass-weighted normal coordinates that diagonalize the quadratic forms, so the motion decomposes into independent harmonic oscillators.

4.4 Semiclassical Tunneling (Wentzel–Kramers–Brillouin)

For a one-dimensional barrier with classical turning points $a < b$ defined by $U(a) = U(b) = E$ and $U(x) > E$ for $a < x < b$, the WKB transmission probability is

$$T \approx \exp\left(-2 \int_a^b \kappa(x) dx\right), \quad \kappa(x) = \frac{\sqrt{2m [U(x) - E]}}{\hbar}, \quad (29)$$

valid when the de Broglie wavelength varies slowly, for example when $\left|\frac{1}{\kappa^2} \frac{d\kappa}{dx}\right| \ll 1$. In that semiclassical regime the WKB method gives an asymptotic expansion in powers of \hbar ; the expression above should be read as the leading exponential factor, with turning-point connection formulas providing prefactors. In multiple dimensions, the integral is replaced by a bounce (instanton) action in imaginary time.

Worked Example 4.1 (Square barrier tunneling estimate). **High-level idea.** We estimate how often an electron can tunnel through a simple rectangular barrier, using the WKB formula in Eq. (29). This puts a concrete numerical scale on the “one-percent” transmission often sketched in barrier diagrams.

Derivation. Consider an electron of mass m_e incident on a square barrier of height $U_0 = 1 \text{ eV}$ and width $L = 0.5 \text{ nm}$, with kinetic energy $E = 0.2 \text{ eV}$. Inside the barrier ($0 < x < L$) we have $U(x) = U_0$ and $U_0 > E$, so $\kappa(x)$ is constant:

$$\kappa = \frac{\sqrt{2m_e (U_0 - E)}}{\hbar}. \quad (30)$$

The integral in Eq. (29) simplifies to

$$\int_a^b \kappa(x) dx = \kappa L, \quad (31)$$

so the WKB transmission becomes

$$T \approx \exp(-2\kappa L). \quad (32)$$

Insert numerical values, converting electronvolts to joules:

$$m_e \approx 9.11 \times 10^{-31} \text{ kg}, \quad (33)$$

$$U_0 - E = 0.8 \text{ eV} \approx 0.8 \times 1.60 \times 10^{-19} \text{ J}, \quad (34)$$

$$\hbar \approx 1.05 \times 10^{-34} \text{ J s}, \quad (35)$$

$$L = 0.5 \times 10^{-9} \text{ m}. \quad (36)$$

From Eq. (30) this gives

$$\kappa = \frac{\sqrt{2m_e(U_0 - E)}}{\hbar} \approx 4.6 \times 10^9 \text{ m}^{-1}, \quad \kappa L \approx 2.3. \quad (37)$$

Using Eq. (32),

$$T \approx \exp(-2\kappa L) \approx \exp(-4.6) \approx 1.0 \times 10^{-2}. \quad (38)$$

Thus, even though $E < U_0$, the electron tunnels through the barrier with probability of order one percent per attempt, which matches the qualitative statements in Sec. 4.4 and the tunneling diagram in Fig. 3. Strictly speaking, an idealized square barrier has discontinuous edges and therefore falls slightly outside the strict smoothness assumptions of WKB, but the exponential factor above coincides with the exact quantum-mechanical result; one can always imagine smoothing the barrier edges on a scale small compared to L .

4.5 Transition-State Theory (TST) and Kramers Escape

On a multi-dimensional potential energy surface (PES), the *transition state* is a saddle with exactly one unstable direction. In its thermodynamic (Eyring) form [4], canonical TST gives

the rate

$$k_{\text{TST}} = \kappa_{\text{TST}} \frac{k_{\text{B}}T}{h} \exp\left(-\frac{\Delta G^{\ddagger}}{k_{\text{B}}T}\right), \quad (39)$$

where ΔG^{\ddagger} is the Gibbs free energy of activation and $0 < \kappa_{\text{TST}} \leq 1$ is the transmission coefficient that corrects for dynamical recrossings of the dividing surface. The factor $k_{\text{B}}T/h$ sets a universal attempt frequency. In a statistical-mechanical derivation, ΔG^{\ddagger} is obtained from the ratio of partition functions for the transition-state region and reactants via the usual relations between free energy and the canonical partition function; TST further assumes quasi-equilibrium between reactants and the transition-state region and a dividing surface chosen with minimal recrossing.

For thermally activated barrier crossing in a one-dimensional potential $U(x)$ subject to viscous drag γ , Kramers' original treatment [7] begins from the Langevin equation

$$m\ddot{x} + \gamma\dot{x} + U'(x) = \xi(t), \quad (40)$$

where $\xi(t)$ is a random force with $\langle \xi(t) \rangle = 0$ and $\langle \xi(t)\xi(t') \rangle = 2\gamma k_{\text{B}}T \delta(t - t')$, ensuring equilibration at temperature T . In the overdamped limit (inertia negligible compared to friction) and for a high barrier $\Delta U \gg k_{\text{B}}T$, the escape rate from a metastable well is

$$k \approx \frac{\omega_0 \omega_b}{2\pi\gamma} \exp\left(-\frac{\Delta U}{k_{\text{B}}T}\right), \quad (41)$$

where $\omega_0^2 = U''(x_{\min})/m$ at the well minimum and $\omega_b^2 = |U''(x_{\text{barrier}})|/m$ at the barrier top. This expression arises in the regime where intrawell relaxation is fast compared to escape and the motion is diffusive near the barrier. In the underdamped regime, prefactors differ (and depend explicitly on the damping) but the Arrhenius exponential persists.

4.6 Electrostatics of a p–n Junction: Built-in Potential and Width

Let $x = 0$ be the metallurgical junction, with acceptor density N_A on $x < 0$ and donor density N_D on $x > 0$. In the depletion approximation [9], Poisson's equation

$$\frac{d^2\varphi}{dx^2} = -\frac{\rho(x)}{\varepsilon_s} = \begin{cases} +\frac{eN_A}{\varepsilon_s}, & -x_p < x < 0, \\ -\frac{eN_D}{\varepsilon_s}, & 0 < x < x_n, \\ 0, & \text{otherwise,} \end{cases} \quad (42)$$

with charge neutrality $N_A x_p = N_D x_n$, integrates to the built-in potential and depletion width

$$V_{bi} = \frac{k_B T}{e} \ln\left(\frac{N_A N_D}{n_i^2}\right), \quad W = x_p + x_n = \sqrt{\frac{2\varepsilon_s V_{bi}}{e} \left(\frac{1}{N_A} + \frac{1}{N_D}\right)}. \quad (43)$$

Here ε_s is the semiconductor permittivity and $e > 0$ is the magnitude of the elementary charge. In the depletion region, the space charge density is due to ionized acceptors and donors, $\rho(x) \approx -eN_A$ for $-x_p < x < 0$ and $\rho(x) \approx +eN_D$ for $0 < x < x_n$, which leads to the explicit signs in Eq. (42). Within the depletion approximation we neglect mobile carriers in $-x_p < x < x_n$ and treat the ionized dopant densities N_A and N_D as uniform.

Worked Example 4.2 (Numerical silicon junction). **High-level idea.** We connect the abstract formulas in Eq. (43) to the band diagram in Fig. 4 by computing the built-in voltage and depletion width for a realistic silicon p–n junction.

Derivation. Take a silicon junction at $T = 300$ K with equal doping $N_A = N_D = 10^{16}$ cm $^{-3}$ and intrinsic carrier concentration $n_i \approx 1.5 \times 10^{10}$ cm $^{-3}$, as in standard textbook examples. First convert to SI units:

$$10^{16} \text{ cm}^{-3} = 10^{22} \text{ m}^{-3}, \quad 1.5 \times 10^{10} \text{ cm}^{-3} = 1.5 \times 10^{16} \text{ m}^{-3}. \quad (44)$$

The built-in potential is

$$V_{bi} = \frac{k_B T}{e} \ln\left(\frac{N_A N_D}{n_i^2}\right). \quad (45)$$

Using $k_B \approx 1.38 \times 10^{-23}$ J/K, $T = 300$ K and $e \approx 1.60 \times 10^{-19}$ C gives

$$\frac{k_B T}{e} \approx 25.9 \text{ mV}, \quad (46)$$

and

$$\ln\left(\frac{N_A N_D}{n_i^2}\right) = \ln\left(\frac{(10^{22})^2}{(1.5 \times 10^{16})^2}\right) \quad (47)$$

$$= \ln(4.4 \times 10^{11}) \approx 26.8. \quad (48)$$

Hence

$$V_{bi} \approx (25.9 \text{ mV}) \times 26.8 \approx 0.69 \text{ V}. \quad (49)$$

For the depletion width, Eq. (43) becomes, with $N_A = N_D$,

$$W = \sqrt{\frac{4\varepsilon_s V_{bi}}{e N_A}}. \quad (50)$$

Using $\varepsilon_s \approx 11.7 \varepsilon_0$ with $\varepsilon_0 \approx 8.85 \times 10^{-12}$ F/m and $N_A = 10^{22} \text{ m}^{-3}$, we obtain

$$W \approx 4.2 \times 10^{-7} \text{ m} \approx 0.42 \mu\text{m}. \quad (51)$$

So for a moderately doped silicon junction, the built-in barrier height in the band diagram is of order 0.7 V and the depletion width is a few tenths of a micron, consistent with the scales sketched in Fig. 4.

4.7 Josephson Junction Dynamics

RCSJ model, plasma frequency, and escape.

For a current-biased junction with capacitance C and shunt resistance R , the Resistively and Capacitively Shunted Junction (RCSJ) equation for the superconducting phase difference ϕ is [11, 14]

$$C \left(\frac{\Phi_0}{2\pi} \right) \ddot{\phi} + \frac{1}{R} \left(\frac{\Phi_0}{2\pi} \right) \dot{\phi} + I_c \sin \phi = I_b + \xi(t), \quad (52)$$

From current balance to a Newton-like equation. Equation (52) is written in *current* units. Multiplying through by $\Phi_0/2\pi$ (which equals $\hbar/2e$) converts it into an *energy*-unit, Newton-like equation for a “phase particle,”

$$C \left(\frac{\Phi_0}{2\pi} \right)^2 \ddot{\phi} + \frac{1}{R} \left(\frac{\Phi_0}{2\pi} \right)^2 \dot{\phi} + \frac{\partial U(\phi)}{\partial \phi} = \left(\frac{\Phi_0}{2\pi} \right) \xi(t), \quad (53)$$

so the effective “mass” is $m_{\text{eff}} = C(\Phi_0/2\pi)^2$ (and the viscous coefficient is $(\Phi_0/2\pi)^2/R$). This explicit rescaling is why the mass carries the *square* of $\Phi_0/2\pi$.

We therefore identify an effective potential energy landscape $U(\phi)$ such that $\partial U/\partial \phi$ reproduces the restoring and tilt forces.

$$U(\phi) = -E_J \cos \phi - \left(\frac{\Phi_0}{2\pi} \right) I_b \phi, \quad E_J = \left(\frac{\Phi_0}{2\pi} \right) I_c, \quad (54)$$

the “tilted-washboard” potential (see Fig. 5). Writing $i = I_b/I_c$, the small-oscillation (plasma) frequency at a well bottom and the barrier height to the adjacent saddle are

$$\omega_p(i) = \sqrt{\frac{2eI_c}{\hbar C}} (1 - i^2)^{1/4}, \quad \Delta U(i) = 2E_J [\sqrt{1 - i^2} - i \arccos(i)]. \quad (55)$$

Here $\xi(t)$ represents a stochastic current from the thermal environment, typically modeled as Gaussian white noise with $\langle \xi(t) \rangle = 0$ and a white spectrum consistent with the Johnson–Nyquist relation for a resistor at temperature T , in accordance with the fluctuation–dissipation theorem. Thermally activated escape follows Kramers-like forms with ω_p as the attempt frequency; at sufficiently low T , macroscopic quantum tunneling replaces thermal activation.

Worked Example 4.3 (Typical Josephson plasma frequency and barrier height).

High-level idea. We estimate realistic energy and frequency scales for a small current-biased Josephson junction used as a qubit, using the analytical expressions in Eq. (55). This shows that gigahertz plasma frequencies and few-kelvin barrier heights are natural in these devices.

Derivation. Consider a junction with critical current $I_c = 1 \mu\text{A}$ and capacitance $C = 1 \text{ pF}$, biased at a reduced current $i = I_b/I_c = 0.8$.

From Eq. (55), the zero-bias plasma frequency ($i = 0$) is

$$\omega_p(0) = \sqrt{\frac{2eI_c}{\hbar C}}. \quad (56)$$

Using $e \approx 1.60 \times 10^{-19} \text{ C}$, $\hbar \approx 1.05 \times 10^{-34} \text{ Js}$, $I_c = 10^{-6} \text{ A}$ and $C = 10^{-12} \text{ F}$, we find

$$\omega_p(0) \approx 5.5 \times 10^{10} \text{ s}^{-1}, \quad f_p(0) = \frac{\omega_p(0)}{2\pi} \approx 8.8 \text{ GHz}. \quad (57)$$

At bias $i = 0.8$, the plasma frequency is reduced by $(1 - i^2)^{1/4}$:

$$\omega_p(0.8) = \omega_p(0) (1 - 0.8^2)^{1/4} \approx 0.77 \omega_p(0) \approx 4.3 \times 10^{10} \text{ s}^{-1}, \quad (58)$$

so

$$f_p(0.8) = \frac{\omega_p(0.8)}{2\pi} \approx 6.8 \text{ GHz}. \quad (59)$$

The Josephson energy is

$$E_J = \frac{\hbar I_c}{2e} \approx \frac{(1.05 \times 10^{-34} \text{ Js})(10^{-6} \text{ A})}{2(1.60 \times 10^{-19} \text{ C})} \approx 3.3 \times 10^{-22} \text{ J}. \quad (60)$$

From Eq. (55), the barrier height at $i = 0.8$ is

$$\Delta U(0.8) = 2E_J \left[\sqrt{1 - 0.8^2} - 0.8 \arccos(0.8) \right] \approx 5.6 \times 10^{-23} \text{ J}. \quad (61)$$

It is often convenient to quote this as an equivalent temperature and frequency scale:

$$\frac{\Delta U}{k_B} \approx 4.1 \text{ K}, \quad f_{\Delta U} = \frac{\Delta U}{h} \approx 8.5 \times 10^{10} \text{ Hz} \approx 85 \text{ GHz}. \quad (62)$$

Thus, for dilution-refrigerator temperatures in the tens of millikelvin, the junction is deep in the quantum regime where macroscopic quantum tunneling and quantized plasma oscillations are both experimentally accessible, as sketched in Fig. 5.

4.8 Landau Expansions Near Symmetry Breaking

Near a continuous phase transition, a scalar order parameter ψ often admits a Landau expansion

$$U(\psi) = a(T - T_c)\psi^2 + b\psi^4 + \dots, \quad b > 0, \quad (63)$$

so that for $T > T_c$ the minimum is at $\psi = 0$, while for $T < T_c$ the minima bifurcate to $\psi = \pm\sqrt{-a(T - T_c)/2b}$. The Hessian at $\psi = 0$ changes sign at T_c , cleanly connecting curvature to stability and to the emergence of multiple wells. In this simple mean-field picture, fluctuations are neglected and the coefficients a and b are treated as smooth, temperature-independent parameters near T_c .

Worked Example 4.4 (Landau double-well: minima, barrier, and Hessian). **High-level idea.** We explicitly solve for the stationary points of the quartic Landau potential in Eq. (63), classify their stability via the Hessian, and compute the barrier height between the symmetry-broken minima for $T < T_c$. This makes concrete how a single parameter T controls whether the “hill” at $\psi = 0$ is a minimum, a saddle (in higher-dimensional generalizations), or a local maximum on the effective energy landscape.

Derivation. For clarity, define

$$\tau \equiv T - T_c, \quad (64)$$

so that Eq. (63) becomes

$$U(\psi) = a\tau\psi^2 + b\psi^4, \quad b > 0, \quad (65)$$

dropping higher-order terms. Stationary points satisfy

$$\frac{dU}{d\psi} = 0. \quad (66)$$

Differentiating Eq. (65) gives

$$\frac{dU}{d\psi} = 2a\tau\psi + 4b\psi^3 = 2\psi(a\tau + 2b\psi^2). \quad (67)$$

Equation (67)=0 therefore yields

$$\psi = 0 \quad \text{or} \quad a\tau + 2b\psi^2 = 0. \quad (68)$$

The nonzero solutions satisfy

$$\psi^2 = -\frac{a\tau}{2b}, \quad (69)$$

which is only physically meaningful for $\tau < 0$ (that is, $T < T_c$) if $a > 0$ and $b > 0$. In that regime the two symmetry-related minima are

$$\psi_{\pm}(T) = \pm\sqrt{-\frac{a\tau}{2b}} = \pm\sqrt{\frac{a(T_c - T)}{2b}}. \quad (70)$$

This reproduces the standard mean-field scaling $\psi \propto (T_c - T)^{1/2}$.

To classify the stationary points, compute the second derivative

$$\frac{d^2U}{d\psi^2} = 2a\tau + 12b\psi^2. \quad (71)$$

At $\psi = 0$,

$$\left. \frac{d^2U}{d\psi^2} \right|_{\psi=0} = 2a\tau. \quad (72)$$

For $T > T_c$ ($\tau > 0$) this curvature is positive and $\psi = 0$ is a local minimum; for $T < T_c$ ($\tau < 0$) the curvature is negative and $\psi = 0$ becomes a local maximum.

At the nonzero stationary points, use Eq. (69) in Eq. (71):

$$\frac{d^2U}{d\psi^2}\Big|_{\psi=\psi_{\pm}} = 2a\tau + 12b\psi_{\pm}^2 \quad (73)$$

$$= 2a\tau + 12b\left(-\frac{a\tau}{2b}\right) \quad (74)$$

$$= 2a\tau - 6a\tau \quad (75)$$

$$= -4a\tau. \quad (76)$$

For $T < T_c$ we have $\tau < 0$ and $a > 0$, so $-4a\tau > 0$ and the points ψ_{\pm} are genuine minima.

Thus the symmetry-broken phase has two degenerate wells separated by a barrier at $\psi = 0$.

Finally, compute the barrier height $\Delta U(T)$ between $\psi = 0$ and either minimum for $T < T_c$. We have $U(0) = 0$ and

$$U(\psi_{\pm}) = a\tau\psi_{\pm}^2 + b\psi_{\pm}^4. \quad (77)$$

Using Eq. (69),

$$U(\psi_{\pm}) = a\tau\left(-\frac{a\tau}{2b}\right) + b\left(\frac{a^2\tau^2}{4b^2}\right) \quad (78)$$

$$= -\frac{a^2\tau^2}{2b} + \frac{a^2\tau^2}{4b} \quad (79)$$

$$= -\frac{a^2\tau^2}{4b}. \quad (80)$$

The barrier height is the difference between the value at $\psi = 0$ and the minimum:

$$\Delta U(T) = U(0) - U(\psi_{\pm}) = \frac{a^2\tau^2}{4b} = \frac{a^2(T_c - T)^2}{4b}, \quad T < T_c. \quad (81)$$

Thus, in this Landau picture:

- The order parameter scales as $\psi_{\pm} \propto (T_c - T)^{1/2}$ below T_c .
- The barrier height between the two minima scales as $\Delta U \propto (T_c - T)^2$, vanishing continuously at T_c .
- The curvature at $\psi = 0$ changes sign at T_c , capturing the loss of stability of the symmetric configuration.

These algebraic results are the precise counterpart of the schematic double-well energy landscapes used to depict symmetry breaking and phase transitions.

4.9 Minimum-Energy Paths on Multidimensional Surfaces (NEB Sketch)

To locate an energetically favorable pathway between minima on a PES, the Nudged Elastic Band (NEB) method relaxes a discrete string of images $\{\mathbf{R}_i\}$ under forces decomposed into parallel and perpendicular components with respect to the path tangent, schematically

$$\mathbf{F}_i^{\text{NEB}} = -\nabla U(\mathbf{R}_i) \Big|_{\perp} + k \left(\|\mathbf{R}_{i+1} - \mathbf{R}_i\| - \|\mathbf{R}_i - \mathbf{R}_{i-1}\| \right) \hat{\boldsymbol{\tau}}_i \Big|_{\parallel}, \quad (82)$$

thereby finding the minimum-energy path that crosses a first-order saddle (the transition state). Here $\hat{\boldsymbol{\tau}}_i$ is a unit tangent vector to the discretized path at image i , so $(\cdot)_{\perp}$ and $(\cdot)_{\parallel}$ denote projections perpendicular and parallel to $\hat{\boldsymbol{\tau}}_i$, respectively. In climbing-image variants the highest-energy image is further modified so that it converges directly to the saddle point.

Worked Example 4.5 (NEB in a one-dimensional double-well). High-level idea.

We illustrate how NEB identifies a saddle point on a simple double-well potential by considering a one-dimensional problem with three images. In 1D the minimum energy path is trivially the coordinate axis itself, but the algebra makes clear how the perpendicular and parallel projections in Eq. (82) reduce to familiar conditions on forces and spring tensions.

Derivation. Consider the quartic double-well potential

$$U(x) = \frac{\lambda}{4} (x^2 - 1)^2, \quad \lambda > 0, \quad (83)$$

which has minima at $x = -1$ and $x = +1$ and a barrier at $x = 0$. Its derivative is

$$U'(x) = \frac{\lambda}{2} (x^2 - 1) (2x) = \lambda x (x^2 - 1). \quad (84)$$

Thus,

$$U'(x) = 0 \implies x \in \{-1, 0, +1\}, \quad (85)$$

with $x = \pm 1$ minima and $x = 0$ a local maximum (the saddle in 1D).

Now place three NEB images at positions x_0, x_1, x_2 with fixed endpoints

$$x_0 = -1, \quad x_2 = +1, \quad (86)$$

and let x_1 relax. In 1D, the path tangent $\hat{\tau}_i$ is either $+1$ or -1 , and there is no perpendicular subspace. Therefore the projection $-\nabla U(\mathbf{R}_i)|_{\perp}$ in Eq. (82) vanishes identically, and only the spring forces along the line remain. Adapting Eq. (82) to this 1D case gives the NEB force on the middle image as

$$F_1^{\text{NEB}} = k(|x_2 - x_1| - |x_1 - x_0|) \sigma, \quad (87)$$

where $\sigma = \pm 1$ encodes the tangent direction. At convergence we require $F_1^{\text{NEB}} = 0$, which in this symmetric three-image setup reduces to

$$|x_2 - x_1| = |x_1 - x_0|. \quad (88)$$

With $x_0 = -1$ and $x_2 = +1$, this condition implies

$$x_1 = 0, \quad (89)$$

placing the central image exactly at the midpoint between the wells. Because the NEB forces in 1D do not include a component proportional to $-U'(x)$ (there is no perpendicular direction to project onto), one supplements the basic NEB with a “climbing image” modification: for the highest-energy image, one reverses the component of $-\nabla U$ along the path to drive it uphill toward the saddle. In this simple symmetric example, x_1 is both the midpoint and the highest-energy image, and the climbing-image NEB update will converge to the exact saddle at $x = 0$ where $U'(0) = 0$ and $U''(0) < 0$.

This toy calculation shows, in the simplest possible setting, that:

- In one dimension the minimum energy path is trivially the coordinate axis, and NEB reduces to locating the barrier top between two wells.
- The equal-spring-length condition reproduces the intuitive picture that the saddle sits halfway between symmetric wells.
- In higher dimensions, the perpendicular projection $-\nabla U(\mathbf{R}_i)|_{\perp}$ prevents the path from cutting corners, while the spring term controls spacing; the 1D algebra here is the limiting case of that more general construction.

5 Evolution of Diagrammatic Conventions

The potential energy diagram has adapted its form to suit the physics of each era. While the core concept remains, the details of what is plotted and what is represented have changed significantly. The table below summarizes this evolution, highlighting the key features of the diagrams used in different fields and historical periods. This summary provides a bird’s-eye view of the intellectual lineage of this powerful visual tool.

Table 1: A Timeline of Potential Energy Diagram Conventions

Era	Typical Abscissa (Horizontal Axis)	Barrier Style	Motion Indicator	Key Concept/Reference
1850s	Position (x)	Smooth, generic hill	Arrow drawn over the top of the hill	Maxwell's illustrations of stability and oscillation.
1889	Reaction coordinate	Single, sharp peak representing the transition state	Arrow rising from reactants to peak, then falling to products	Arrhenius equation and the concept of activation energy (E_a).
1928	Radial distance in nucleus (r)	Square well plus a decaying Coulomb wall	Arrow pointing directly <i>through</i> the barrier wall	Gamow's theory of alpha decay and quantum tunneling.
1935	Reaction coordinate	A saddle point on a multi-dimensional surface	A curved path or trajectory over the saddle point	Transition State Theory (TST) formalizing the activated complex (\ddagger).
1947	Depth into a semiconductor device	Abrupt steps or gradual bending of energy bands	Arrows indicating electron and hole flow (downhill/uphill)	Early p-n junction and transistor band diagrams.
1985	Superconducting phase difference (ϕ)	Tilted periodic cosine wave (“washboard”)	Arrows showing escape from a potential well	Josephson junction dynamics for qubits and SQUIDs.
2010s	Multi-dimensional Potential Energy Surface (PES)	Color-mapped ridges and valleys on a 2D or 3D plot	Streamlines, tunneling paths, or probability density plots	Modern computational chemistry and quantum dynamics visualizers.

6 Conceptual Connections and Glossary

To synthesize the information, we can visualize the connections between these ideas with a mind map and define the key acronyms in a glossary.

6.1 Mind-Map of Concepts

The various applications of energy diagrams can be organized into a conceptual tree, showing how the core idea has branched into different domains of physics.

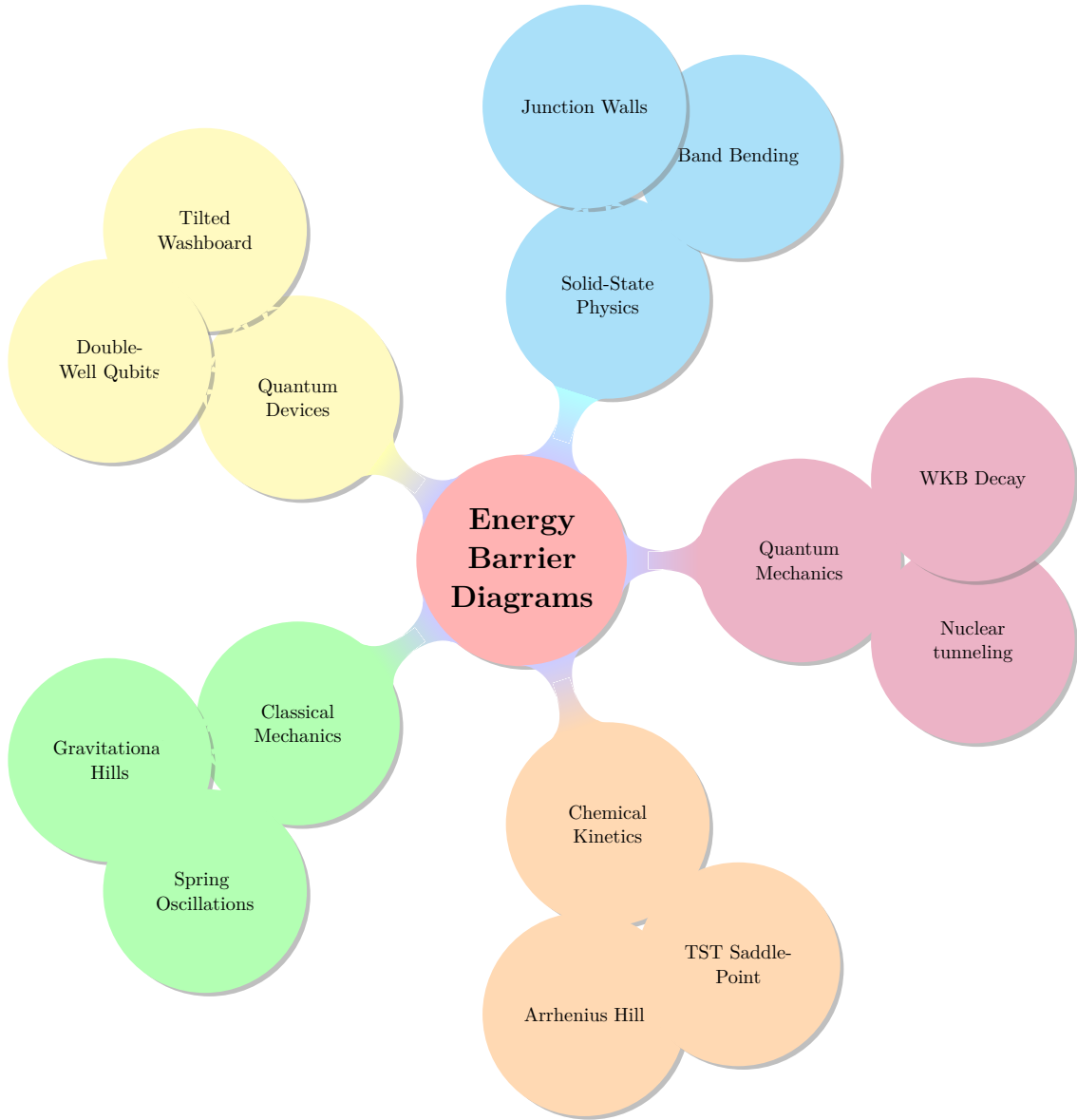


Figure 6: A mind-map illustrating the branching applications of potential energy diagrams across different fields of physics.

6.2 Diagrammatic Cousins: Heat Maps

Potential-energy diagrams are, in a literal sense, one-dimensional plots of a scalar field $U(\mathbf{q})$ evaluated along a chosen coordinate or path. In computational chemistry, condensed matter, and device modeling, the same idea often appears in higher-dimensional form: one visualizes a scalar field on a plane or volume using color, contours, and gradients. *Heat maps* are one widely used visual language for this purpose. They are not “energy barrier diagrams” in

the strict historical sense, but they share the same representational core: a scalar landscape whose peaks, valleys, and passes encode stability, transition pathways, and sensitivity.

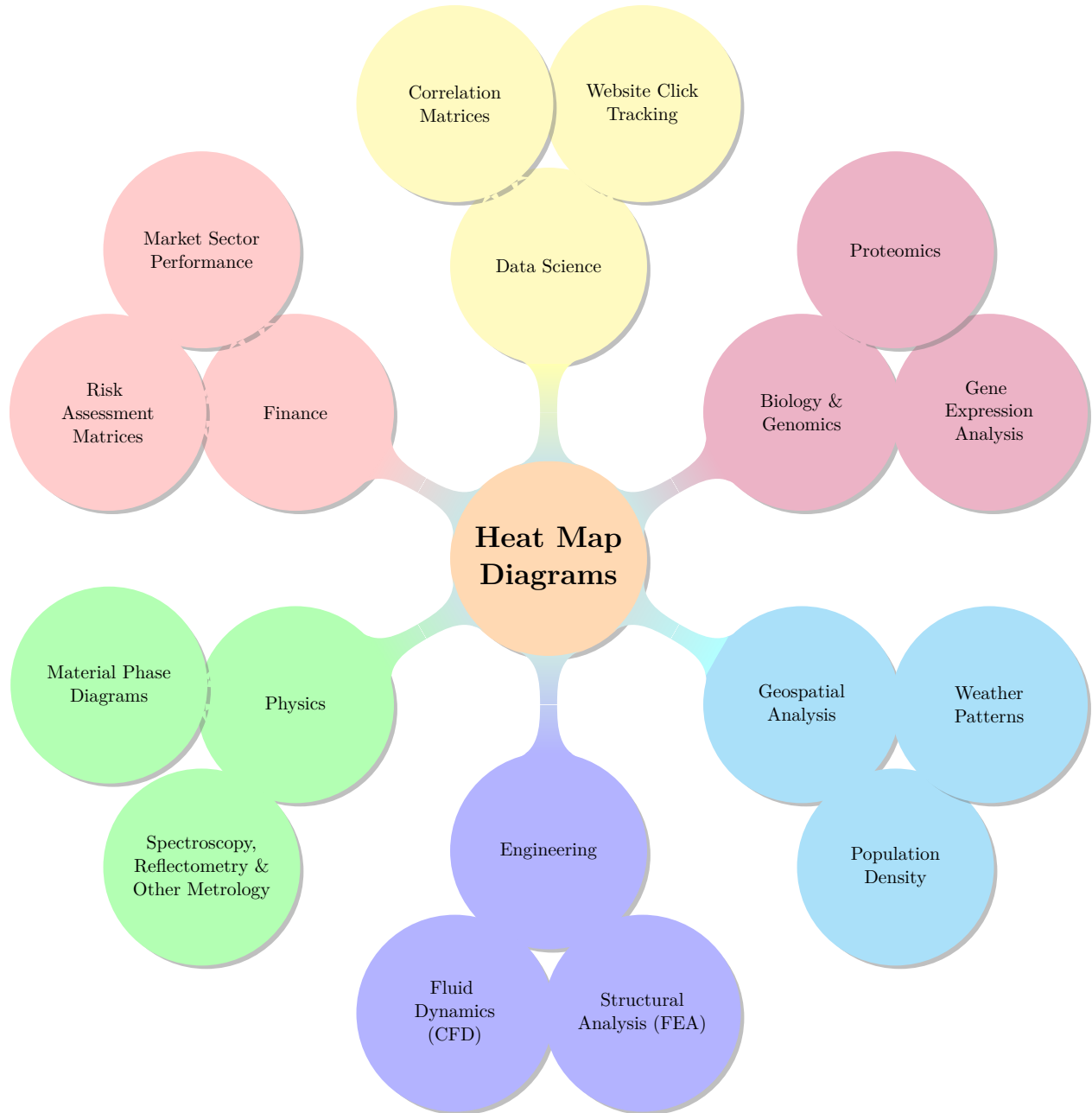


Figure 7: An additional mind-map illustrating the broad, cross-disciplinary applications of heat map diagrams.

7 Formula Sheet: Barriers, Rates, and Wells

Table 2: Frequently Used Relations for Potential Energy Barriers and Stability

Topic	Formula	Notes/ Definitions
Force–potential (1D)	$F(x) = -dU/dx$	Conservative force points downhill
Force–potential (ND)	$\mathbf{F}(\mathbf{q}) = -\nabla U(\mathbf{q})$	$\mathbf{q} \in \mathbb{R}^n$
Equilibrium condition	$\nabla U(\mathbf{q}_*) = \mathbf{0}$	Critical points of U
Stability classification	$H = \nabla^2 U(\mathbf{q}_*)$; sign of eigenvalues \Rightarrow min / saddle / max	Morse index = # negative eigenvalues
Small oscillations	$M\ddot{\mathbf{y}} + H\mathbf{y} = 0, \quad H\mathbf{v} = \omega^2 M\mathbf{v}$	Normal modes near a minimum
WKB transmission	$T \approx \exp\left(-2 \int_a^b \kappa(x) dx\right), \quad \kappa(x) = \frac{\sqrt{2m[U(x) - E]}}{\hbar}$	Valid when $\left \frac{1}{\kappa^2} \frac{d\kappa}{dx}\right \ll 1$
TST (Eyring)	$k = \kappa_{\text{TST}} \frac{k_B T}{\hbar} e^{-\Delta G^\ddagger/k_B T}$	$\kappa_{\text{TST}} \leq 1$ corrects recrossings; ΔG^\ddagger Gibbs free energy of activation
Kramers (overdamped)	$k \approx \frac{\omega_0 \omega_b}{2\pi\gamma} e^{-\Delta U/k_B T}$	$\omega_0^2 = U''(x_{\min})/m$, $\omega_b^2 = U''(x_{\text{barrier}}) /m$
p–n built-in potential	$V_{bi} = \frac{k_B T}{e} \ln\left(\frac{N_A N_D}{n_i^2}\right)$	Depletion approximation
p–n depletion width	$W = \sqrt{\frac{2\varepsilon_s V_{bi}}{e}} \left(\frac{1}{N_A} + \frac{1}{N_D}\right)$	$N_A x_p = N_D x_n$
JJ potential (biased)	$U(\phi) = -E_J \cos \phi - \frac{\hbar I_b}{2e} \phi, \quad E_J = \frac{\hbar I_c}{2e}$	Tilted washboard
JJ plasma frequency	$\omega_p(i) = \sqrt{\frac{2eI_c}{\hbar C}} (1 - i^2)^{1/4}, \quad i = I_b/I_c$	Small oscillations at well bottom
JJ barrier height	$\Delta U(i) = 2E_J [\sqrt{1 - i^2} - i \arccos(i)]$	Height to adjacent saddle
Landau expansion	$U(\psi) = a(T - T_c)\psi^2 + b\psi^4 + \dots$	Curvature sign flip at T_c

7.1 Acronym Glossary

Table 3: Glossary of Common Acronyms and Symbols

Acronym	Full Expression	Context
PES	Potential Energy Surface	Multidimensional landscapes for molecules, solids, devices
TST	Transition State Theory	Rate theory at a first-order saddle on a PES
WKB	Wentzel–Kramers–Brillouin	Semiclassical tunneling approximation
NEB	Nudged Elastic Band	Minimum-energy path algorithm on a PES
JJ	Josephson Junction	Superconducting weak link forming a nonlinear potential
RCSJ	Resistively and Capacitively Shunted Junction	Dynamical model for current-biased JJs
MQT	Macroscopic Quantum Tunneling	Quantum escape of a collective coordinate (e.g., JJ phase)
SQUID	Superconducting Quantum Interference Device	Interferometric magnetometer based on JJs
MOSFET	Metal–Oxide–Semiconductor Field-Effect Transistor	Semiconductor device, band-bending control
V_{bi}	Built-in Potential	p-n junction barrier at equilibrium
W	Depletion Width	Total width $x_p + x_n$ of the space-charge region
ω_p	Plasma Frequency	Small-oscillation frequency in a JJ well
ΔU	Barrier Height	Energy difference between a well minimum and the adjacent saddle

8 Conclusion: A Representation Agnostic Vision

From the simple act of a ball rolling down a hill to the probabilistic leap of a quantum particle through a barrier, the potential energy diagram has provided physicists with a powerful and unifying way to visualize and understand the dynamics of physical systems. Its strength lies in its simplicity and its deep connection to our everyday intuition about energy and motion. By mapping abstract concepts like reaction coordinates or quantum phases onto a familiar graphical landscape, it makes the invisible visible and the complex comprehensible.

The evolution of this diagram is a story of scientific progress itself. Each new domain of physics, from classical mechanics to quantum computing, has adapted the tool for its own purposes, adding new layers of sophistication while retaining the core metaphor. We have seen how the simple hill of classical mechanics becomes the activation barrier of chemistry, the tunneling wall of quantum mechanics, the bent bands of semiconductor physics, and the tilted washboard of quantum computing. We have also explored the rigorous mathematical framework of stability that underlies these intuitive pictures, and extended the discussion to double-well qubits and metamaterial-based quantum transducers where effective potentials guide photons and phonons.

The arrows may now point *through* the hills as often as they point *over* them, and the landscape may be a multi-dimensional, computer-generated surface rather than a simple hand-drawn curve. Yet, the fundamental idea remains unchanged. Physicists continue to rely on these gravity-inspired sketches to portray the energetic cost of crossing from “here” to “there.” Whether the traveler is a reacting molecule, a tunneling alpha particle, a drifting electron, a macroscopic quantum phase, or an engineered optical or mechanical mode, the diagram’s hill captures both the challenge and the creativity of the journey, proving its status as one of the most enduring and effective conceptual tools in all of science.

Selected References

- [1] J.-L. Lagrange, *Mécanique analytique*, Paris (1788).
- [2] J. C. Maxwell, *Matter and Motion*, Society for Promoting Christian Knowledge, London (1873).
- [3] S. Arrhenius, “Über die Reaktionsgeschwindigkeit bei der Inversion von Rohrzucker durch Säuren,” *Z. Phys. Chem.* **4**, 226–248 (1889).
- [4] H. Eyring, “The Activated Complex in Chemical Reactions,” *J. Chem. Phys.* **3**, 107–115 (1935).
- [5] G. Gamow, “Zur Quantentheorie des Atomkernes,” *Z. Phys.* **51**, 204–212 (1928).
- [6] R. W. Gurney and E. U. Condon, “Quantum Mechanics and Radioactive Disintegration,” *Phys. Rev.* **33**, 127–140 (1929).
- [7] H. A. Kramers, “Brownian motion in a field of force and the diffusion model of chemical reactions,” *Physica* **7**, 284–304 (1940).
- [8] W. Shockley, *Electrons and Holes in Semiconductors*, D. Van Nostrand, New York (1950).
- [9] S. M. Sze and K. K. Ng, *Physics of Semiconductor Devices*, 3rd ed., Wiley, Hoboken (2006).
- [10] B. D. Josephson, “Possible new effects in superconductive tunnelling,” *Phys. Lett.* **1**, 251–253 (1962).
- [11] M. Tinkham, *Introduction to Superconductivity*, 2nd ed., McGraw–Hill, New York (1996).
- [12] L. D. Landau and E. M. Lifshitz, *Statistical Physics, Part 1*, 3rd ed., Pergamon, Oxford (1980).

- [13] L. D. Landau and E. M. Lifshitz, *Course of Theoretical Physics, Vol. 5: Statistical Physics*, Pergamon, Oxford (1958).
- [14] A. M. Zagoskin, *Quantum Engineering: Theory and Design of Quantum Coherent Structures*, Cambridge Univ. Press, Cambridge (2011).
- [15] Y. Meng *et al.*, “Optical meta-waveguides for integrated photonics and beyond,” *Light: Science & Applications* **10**, 214 (2021).
- [16] X. Han *et al.*, “Microwave-optical quantum frequency conversion,” *Optica* **8**, 1050–1064 (2021).

License

Creative Commons Attribution 4.0 International (CC BY 4.0)

© 2025 Onri Jay Benally

This work is licensed under a Creative Commons “Attribution 4.0 International” license.



This work is licensed under the Creative Commons Attribution 4.0 International (CC BY 4.0). You are free to share and adapt the material for any purpose, even commercially, provided that you give appropriate credit, provide a link to the license, and indicate if changes were made. No additional restrictions apply beyond those of the license.

License URL: <https://creativecommons.org/licenses/by/4.0/>

Attribution (preferred citation):

Onri Jay Benally, *A Treatise on Potential Energy Diagrams in Physics: A Historical and Pedagogical Review*, August 2025, Creative Commons Attribution 4.0 International (CC BY 4.0).